cmgh
CELLULAR AND MOLECULAR GASTROENTEROLOGY AND HEPATOLOGY

ORIGINAL RESEARCH

Enteroendocrine Cells Protect the Stem Cell Niche by Regulating Crypt Metabolism in Response to Nutrients

Heather A. McCauley,[1,2,3] Anne Marie Riedman,[1,2] Jacob R. Enriquez,[1,2] Xinghao Zhang,[1,2] Miki Watanabe-Chailland,[4] J. Guillermo Sanchez,[1,2] Daniel O. Kechele,[1,2] Emily F. Paul,[1,2] Kayle Riley,[1,2,5] Courtney Burger,[6] Richard A. Lang,[1,6] and James M. Wells[1,2,7]

[1]Division of Developmental Biology, Cincinnati Children's Hospital Medical Center, Cincinnati, Ohio; [2]Center for Stem Cell and Organoid Medicine, Cincinnati Children's Hospital Medical Center, Cincinnati, Ohio; [3]Department of Cell Biology and Physiology, University of North Carolina at Chapel Hill, School of Medicine, Chapel Hill, North Carolina; [4]Nuclear Magnetic Resonance-Based Metabolomics Core Facility, Division of Pathology and Laboratory Medicine, Cincinnati Children's Hospital Medical Center, Cincinnati, Ohio; [5]Postbaccalaureate Research Education Program, University of Cincinnati College of Medicine, Cincinnati, Ohio; [6]The Visual Systems Group, Abrahamson Pediatric Eye Institute, Division of Pediatric Ophthalmology, Cincinnati Children's Hospital Medical Center, Cincinnati, Ohio; and [7]Division of Endocrinology, Cincinnati Children's Hospital Medical Center, Cincinnati, Ohio

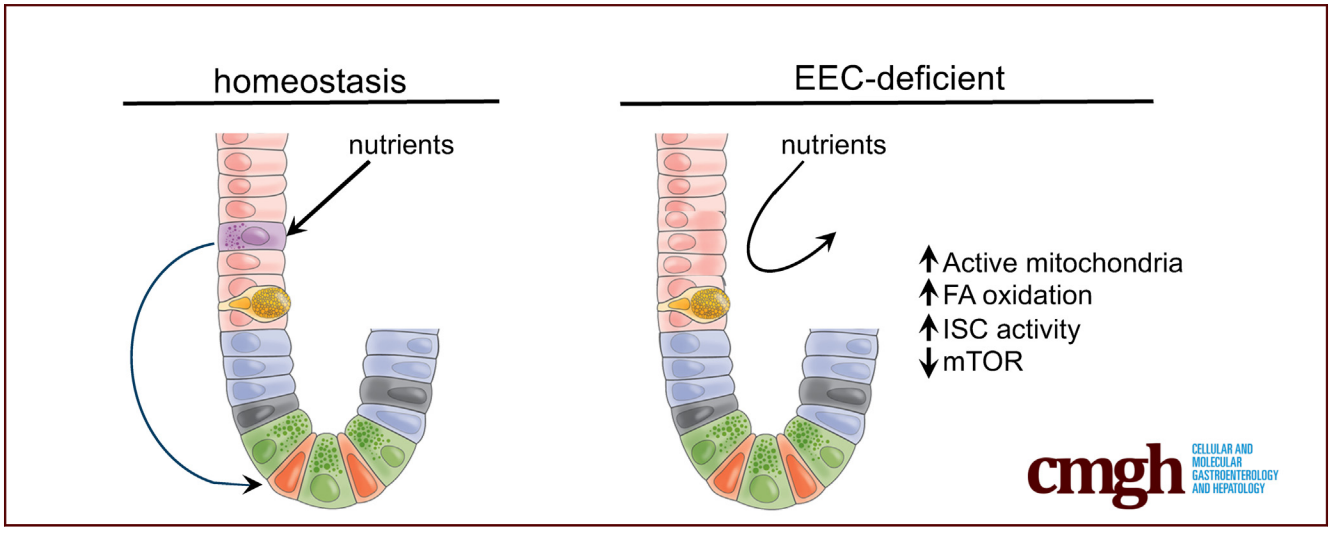

SUMMARY

In this study, loss of enteroendocrine cells recapitulated many aspects of fasting, including increased stem and progenitor activity, increased fatty acid oxidation, and loss of activity of mammalian target of rapamycin signaling in intestinal crypts. These data suggest that enteroendocrine cells are essential regulators of intestinal metabolism and crypt homeostasis.

BACKGROUND & AIMS: The intestinal stem cell niche is exquisitely sensitive to changes in diet, with high-fat diet, caloric restriction, and fasting resulting in altered crypt metabolism and intestinal stem cell function. Unlike cells on the villus, cells in the crypt are not immediately exposed to the dynamically changing contents of the lumen. We hypothesized that enteroendocrine cells (EECs), which sense environmental cues and in response release hormones and metabolites, are essential for relaying the luminal and nutritional status of the animal to cells deep in the crypt.

METHODS: We used the tamoxifen-inducible *VillinCreERT2* mouse model to deplete EECs (*Neurog3*$^{fl/fl}$) from adult intestinal epithelium and we generated human intestinal organoids from wild-type and NEUROGENIN 3 (NEUROG3)-null human pluripotent stem cells. We used indirect calorimetry, ^{1}H-Nuclear Magnetic Resonance (NMR) metabolomics, mitochondrial live imaging, and the Seahorse bioanalyzer (Agilent Technologies) to assess metabolism. Intestinal stem cell activity was measured by proliferation and enteroid-forming capacity. Transcriptional changes were assessed using 10x Genomics single-cell sequencing.

RESULTS: Loss of EECs resulted in increased energy expenditure in mice, an abundance of active mitochondria, and a shift of crypt metabolism to fatty acid oxidation. Crypts from mouse and human intestinal organoids lacking EECs displayed increased intestinal stem cell activity and failed to activate phosphorylation of downstream target S6 kinase ribosomal protein, a marker for activity of the master metabolic regulator mammalian target of rapamycin (mTOR). These phenotypes were similar to those observed when control mice were deprived of nutrients.

CONCLUSIONS: EECs are essential regulators of crypt metabolism. Depletion of EECs recapitulated a fasting metabolic phenotype despite normal levels of ingested nutrients. These data suggest that EECs are required to relay nutritional information to the stem cell niche and are essential regulators of intestinal metabolism. *(Cell Mol Gastroenterol Hepatol 2023; 15:1293–1310; https://doi.org/10.1016/j.jcmgh.2022.12.016)*

Keywords: Enteroendocrine Cells; Intestinal Metabolism; Mitochondria; Intestinal Stem Cell.

Oral nutrients are required to fuel all cellular and systemic functions throughout the body. The gastrointestinal tract digests and absorbs carbohydrates, proteins, fats, and micronutrients, which then pass into the circulation to be used by other organs. However, as the initial site of nutrient sensing and nutrient absorption, the intestinal epithelium must first fuel itself to then be able to power the rest of the body. In fact, 20%–25% of the body's entire metabolic demand occurs within the intestine.[1]

The large metabolic demand of the mammalian small intestine is in part owing to the fact that the epithelium is regenerated every approximately 5 days from highly proliferative intestinal stem cells that reside in the crypts of Lieberkühn.[2] Intestinal stem cells give rise to daughter progenitor cells that go through several rounds of proliferation as they migrate upward through the transit-amplifying zone while committing into the absorptive or secretory lineages in the terminally differentiated villus epithelium.[2] Some enteroendocrine cells (EECs) and all Paneth cells instead migrate downward into the crypt region where a complex orchestra of secreted factors from epithelial and mesenchymal cells function as the intestinal stem cell niche.[2]

EECs of the gut represent the largest endocrine organ in the body, and one of their primary functions is to sense environmental cues such as luminal nutrients and metabolites.[3] In response to these diverse inputs, EECs secrete more than 20 distinct hormones, numerous other bioactive peptides, and small metabolites such as adenosine triphosphate (ATP).[4] The secreted products of EECs enter systemic circulation, interact with the enteric and central nervous systems, and exert paracrine effects on local targets within the gut itself.[3,4] Despite their rarity, EECs are essential for several intestinal functions. Congenital loss of EECs results in failure to thrive and malabsorptive diarrhea upon ingestion of oral nutrition in human beings[5] and mice.[6,7] We previously reported that EECs were required to maintain the electrophysiology supporting nutrient absorption in the small intestine,[7] placing EECs in a central role regulating basic cell biological functions of their neighboring enterocytes.

The diverse cellular functions that intestinal epithelial cells perform are supported by a range of cellular metabolic pathways.[8] Absorptive enterocytes are the most abundant cell type of the small intestine and primarily absorb nutrients and water. Macronutrient absorption and trafficking are energetically demanding processes, and, as such, enterocytes contain abundant mitochondria and largely use oxidative phosphorylation.[8–10] Similar to most proliferative zones in the body, intestinal crypts generate most of their energy via glycolysis.[9–11] However, healthy mitochondria, which perform numerous functions such as reactive oxygen species production, cell death, and activation of biosynthetic pathways, in addition to energy production, are essential for proper intestinal stem cell function and differentiation into mature cell types.[11–16] Mitochondrial activity is higher in intestinal stem cells than in Paneth cells, and the metabolites lactate[13] and pyruvate[11] produced by glycolysis in Paneth cells have been shown to serve as important niche factors for intestinal stem cell function. Moreover, loss of the mitochondrial chaperone protein *Hsp60*[12] or of the transcription factor YY,[16] which is required for expression of mitochondrial complex I genes, resulted in loss of intestinal stem cell numbers and activity. Together, these studies show that although oxidative phosphorylation is not the dominant source of energy for the crypt as a whole, mitochondria are essential in maintaining intestinal stem cell function.

Crypt metabolism and intestinal stem cell function are exquisitely sensitive to changes in diet.[17–21] Intriguingly, when mice are fasted[21] or fed a high-fat diet,[17,18] intestinal stem cells respond by up-regulating mitochondrial fatty acid oxidation. In times of fat excess, the intestinal stem cell uses available nutrients to maximize efficiency of nutrient availability. Conversely, in times of nutrient deprivation, the intestinal stem cell shifts to fatty acid oxidation as a protective mechanism to preserve intestinal function.[21] Because cells deep within the crypt are far removed from the high nutritional environment of the lumen, we hypothesized that a nutrient-sensing cell such as the enteroendocrine cell may be involved in crypt adaptations to nutrient availability.

In this study, we identified a new role for EECs in regulating the cellular metabolism of the crypt. We found that acute loss of EECs increased mitochondrial activity and fatty acid oxidation in whole intestinal crypts, resulting in increased intestinal stem cell activity in mouse small intestine and human intestinal organoids. Loss of EECs recapitulated many aspects of fasting, including loss of activity of mammalian target of rapamycin (mTOR) signaling. mTOR signaling is the main downstream sensor of availability of nutrients, guiding stem cells in many organs to adjust to nutritional availability. Together, our data suggest that EECs are essential regulators of crypt metabolism and intestinal stem cell homeostasis.

Abbreviations used in this paper: **ADP, adenosine diphosphate; ATP, adenosine triphosphate; EEC, enteroendocrine cell; FBS, fetal bovine serum; GLP-1, glucagon-like peptide 1; ^{1}H-NMR, 1H-Nuclear Magnetic Resonance; IBD, inflammatory bowel disease; ISC, intestinal stem cell; mTOR, mammalian target of rapamycin; mTORC1, mammalian target of rapamycin complex 1; OLFM4, olfactomedin-4; PBS, phosphate-buffered saline; PCR, polymerase chain reaction; phospho-S6, phosphorylation of downstream target S6 kinase; scRNA, single-cell RNA; TMRM, tetramethylrhodamine methyl ester; VCO_2, carbon dioxide emission; VO_2, oxygen consumption.**

Most current article

© 2023 The Authors. Published by Elsevier Inc. on behalf of the AGA Institute. This is an open access article under the CC BY-NC-ND license (http://creativecommons.org/licenses/by-nc-nd/4.0/).
2352-345X
https://doi.org/10.1016/j.jcmgh.2022.12.016

Results

Conditional Loss of EECs Alters Whole-Body and Intestinal Metabolism Within Days

To investigate the role of EECs in intestinal homeostasis and metabolism, we depleted EECs from the intestinal epithelium in adult mice. Congenital loss of EECs results in malabsorptive diarrhea with poor postnatal survival,[6,7] so to circumvent this obstacle we crossed *Neurogenin3 (Neurog3)*$^{fl/fl}$ animals with the tamoxifen-inducible *Villin-CreERT2*[22] and induced deletion when mice were 8–12 weeks of age (Figure 1*A*). Because of the well-known toxicity of tamoxifen to the stem cells of the gastrointestinal tract,[23] we analyzed mice 10 days after tamoxifen administration after stem cells had recovered from this injury. At 10 days, *Neurog3*$^{fl/fl}$ animals displayed no outward signs of poor health, no significant change in weight, and fecal pellets were well formed. However, upon internal examination, the jejunum, ileum, cecum, and proximal colon were distended and filled with liquid contents (Figure 1*B* and *C*). This internal diarrhea did not affect transit time in the small bowel (Figure 1*D*). At this time point, EECs were diminished from the midjejunum by 96%, with a corresponding reduction in hormone transcripts and proteins (Figure 1*E*–*I*). We used the tdTomato Ai9 reporter allele[24] to monitor for Cre recombination efficiency. We reasoned that the poor efficiency of the *Villin* promotor in the distal colon[25] (Figure 1*H*) allowed for adequate water resorption and the formation of solid feces despite the proximal liquid enteral contents. The gross phenotype of the small bowel suggested that loss of EECs disrupted intestinal physiology and function in the adult animal.

EECs have a well-established role in regulating many aspects of systemic metabolism. To determine whether loss of EECs impacted whole-body metabolism, control *VillinCreERT2* and *VillinCreERT2;Neurog3*$^{fl/fl}$ animals were housed in metabolic cages for assessment by indirect calorimetry (Figure 1*L*). During the period of acclimation, there was no difference in any parameter measured between genotypes; however, approximately 1 day after the first dose of tamoxifen, *Villin-CreERT2;Neurog3*$^{fl/fl}$ animals began to increase their total energy expenditure over control animals (Figure 1*J*). This difference in energy expenditure, calculated by the abbreviated Weir equation as an additive function of oxygen consumption and carbon dioxide production, continued to increase for the course of the 10-day experiment. There was no difference in food consumed or activity between control and EEC-deficient groups (Figure 1*K* and *L*), suggesting the increased energy expenditure occurred primarily at the cellular level.

Considering that the intestine is a major metabolic organ, consuming approximately 20%–25% of the body's total oxygen requirements,[1] we investigated whether loss of EECs would impact cellular metabolism within the intestine directly. Because EECs have a well-established link to the microbiome, we performed ^{1}H-Nuclear Magnetic Resonance (NMR) metabolomic profiling on fecal pellets as well as epithelial cells isolated from control and EEC-deficient jejunum (Figure 2*A* and *B*). Forty-three unique metabolites were quantified from the fecal samples. A principal component analysis showed significant overlap between samples collected from control and EEC-deficient animals (Figure 2*A*). Notably, there was no significant difference between short-chain fatty acids acetate, butyrate, or propionate, metabolites produced by the microbiome that in turn are sensed by EECs. We concluded that, under these experimental conditions, loss of EECs had a minimal effect on microbial metabolism. We next analyzed jejunal epithelial cells by ^{1}H-NMR (Figure 2*B*–*D*). Because there are well-defined metabolic differences in cellular metabolism between crypts and villi,[9] we separated these compartments for our analysis. Thirty-four unique metabolites were identified and quantified (Figure 2*B*–*D*), and a principal component analysis showed significant overlap between control and EEC-deficient villus samples. However, EEC-deficient crypts clustered distinctly from control crypts, clustering closer to the villus samples (Figure 2*B*). Two of the significant metabolites altered in EEC-deficient crypts compared with control were adenosine triphosphate (ATP) and adenosine diphosphate (ADP) (Figure 2*C*). In control animals, ATP was higher in the crypt than in the villus, consistent with the glycolytic nature of the highly proliferative crypt compartment.[9] Loss of EECs resulted in significant reduction of both ATP and ADP in the crypt compared with control crypts (Figure 2*C*). In EEC-deficient samples, crypt ATP was reduced to villus levels, whereas ADP was very low or not detected at all (Figure 2*C*). These data suggest that EECs are required for normal cellular metabolism along the crypt–villus axis, and that in the absence of EECs, the crypt adopts a metabolic profile more closely resembling that of the villus.

EECs Regulate Mitochondrial Activity in Intestinal Crypts

EEC-deficient crypts adopted a more villus-like metabolic profile (Figure 2*B*), which predominantly use mitochondrial oxidative phosphorylation to meet energetic demands.[9] To investigate this further we assessed mitochondrial activity by a live-imaging approach using tetramethylrhodamine methyl ester (TMRM), a fluorescent readout of mitochondrial activity (Figure 3*A*). Cells in control villi had high mitochondrial activity, and loss of EECs had no obvious impact on villus mitochondrial activity, consistent with ^{1}H-NMR profiling (Figure 2*B*). In comparison with villus preparations, control crypts had low mitochondrial activity as determined by few TMRM+ cells. However, EEC-deficient crypts displayed abundant TMRM+ cells, indicating highly active mitochondria in nearly every crypt cell (Figure 3*A*). Paneth cells, as marked by *Ulex europaeus* Agglutinin 1, were largely negative for TMRM+ active mitochondria. TMRM+ active mitochondria were observed in mice that had undergone tamoxifen-induced depletion of EECs 28 days before analysis (Figure 3*B*), suggesting that the metabolic reprogramming of the intestine was a stable phenotype. Activation of TMRM+ mitochondria did not occur immediately upon loss of *Neurog3*, because at 24 hours post-tamoxifen administration there was no difference between genotypes, but robust TMRM+ activity was observed 3 days after tamoxifen administration (Figure 3*B*). This increase in mitochondrial activity was not

owing to an increase in mitochondrial content because there were no significant changes in gene expression of mitochondrial inner and outer membrane proteins, or protein expression of outer mitochondrial membrane protein Tom20 between genotypes (Figure 3*C*). These data suggested that EECs regulate mitochondrial activity in the crypt.

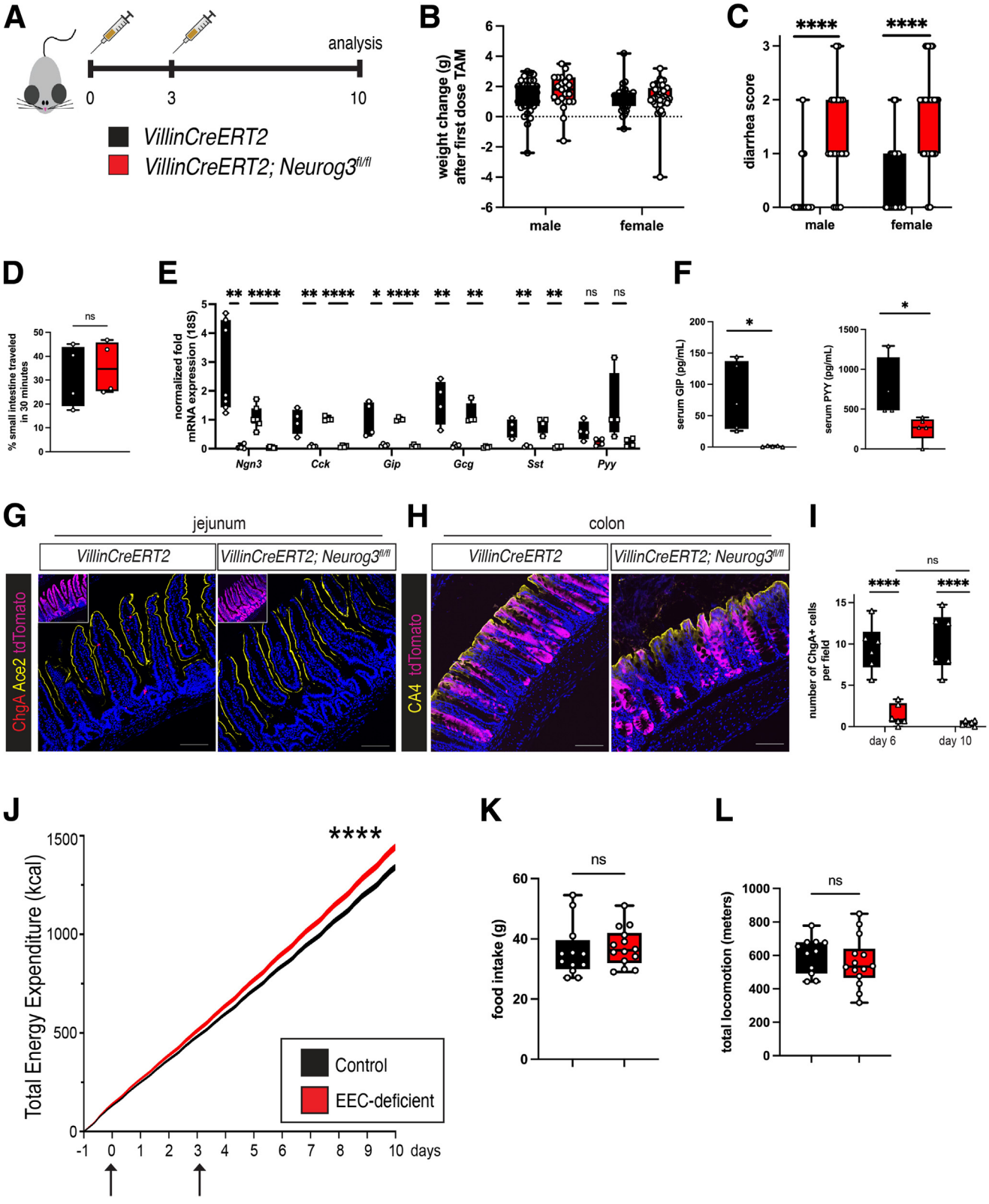

Cells of the crypt can dynamically alter their metabolism in response to changes in nutrient availability. For example, when mice are fasted, the crypt responds by activating mitochondrial fatty acid metabolism to maintain homeostasis in the absence of nutrients.[21] We observed abundant TMRM+ active mitochondria in the crypts of control mice that had been fasted overnight, mimicking the increased mitochondrial activity observed in EEC-deficient crypts (Figure 3*B*). To functionally investigate whether increased TMRM fluorescence correlated with fatty acid oxidation and oxidative phosphorylation, we measured crypt mitochondrial activity using the Seahorse bioanalyzer (Agilent Technologies) (Figure 3*E*). We observed significantly increased basal oxygen consumption in EEC-deficient crypts and in fasted control crypts, consistent with increased mitochondrial activity, compared with fed control crypts. We next cultured crypts in etomoxir, a chemical inhibitor that blocks the entry of fatty acids into mitochondria for oxidation. Control crypts had low levels of basal oxygen consumption, and this was unaffected by treatment with etomoxir. In contrast, the high basal oxygen consumption in EEC-deficient crypts and fasted control crypts were restored to control-fed levels by etomoxir (Figure 3*E*). This indicated that the increased mitochondrial activity observed in the absence of nutrients or in the absence of nutrient-sensing EECs was the result of activation of mitochondrial fatty acid oxidation.

EECs Regulate Intestinal Stem and Progenitor Activity

Crypt metabolism is a major determinant of intestinal stem cell (ISC) function.[9,26] In particular, fasting increases proliferation and enhances ISC activity.[21] We therefore investigated whether the altered crypt metabolism in EEC-deficient animals impacted intestinal stem and progenitor activity. We induced deletion of EECs in 8- to 12-week-old animals and monitored cell proliferation and ISC marker expression 10 days after the first tamoxifen injection. EEC-deficient crypts had increased cell proliferation (Figure 4*A* and *B*) and expanded expression of the stem and progenitor marker olfactomedin 4 (Olfm4)[27] (Figure 4*C*), consistent with fasted control animals. We observed a slight trend toward increased crypt depth (110.7 vs 97.45 mm) and villus height (326.7 vs 290 mm) in EEC-deficient jejunum (Figure 4*D*). There was no change in apoptosis between genotypes (Figure 4*E* and *F*). To determine if the increases in proliferation and Olfm4 expression in the EEC-deficient animals translated into increased ISC activity, we quantified the enteroid-forming capacity of isolated crypts grown in culture. EEC-deficient crypts had 2- to 3-fold higher enteroid-forming capacity than control, consistent with fasted crypts[21] (Figure 4*G*).

The functional role of EECs in regulating human intestinal stem cell activity is unknown. We therefore performed similar analyses of human intestinal organoids lacking EECs. We generated EEC-deficient pluripotent stem cell–derived human intestinal organoids as previously described.[7] Briefly, human pluripotent stem cells were directed to differentiate first into endoderm, and then midhindgut, by application of a series of growth factors mimicking those that the embryo experiences during early gestation.[28] Three-dimensional midhindgut spheroids spontaneously formed, which grew and matured over the course of 28 days

Figure 1. (***See previous page***). **EECs are required to maintain whole-body metabolism.** (*A*) Schematic of tamoxifen (TAM) dosing strategy. Mice aged 8 weeks or older were administered 2 doses of tamoxifen (25 mg/kg) 3 days apart. Animals were harvested 10 days after the initial dose to evaluate loss of EECs. Age-matched, nonlittermate *VillinCreERT2* mice were used as controls. Some animals also carried the Ai9 *Rosa26-*$^{flox\text{-}STOP\text{-}flox\text{-}tdTomato}$ reporter allele to evaluate the efficiency of recombination. (*B*) Body weight of animals dosed with tamoxifen. Statistical significance was determined by 2-way analysis of variance. n = 31 control females, 35 control males, 39 experimental females, and 23 experimental males. (*C*) Diarrhea score of *VillinCreERT2;Neurog3*$^{fl/fl}$ animals (*red bars*) compared with *VillinCreERT2* control animals (*black bars*) dosed with tamoxifen (male, ****$P < .0001$; female, ****$P < .0001$). Notably, many *VillinCreERT2* control animals showed mild diarrhea 10 days after tamoxifen treatment. Statistical significance was determined by 2-way analysis of variance. n = 31 control females, 35 control males, 39 experimental females, and 23 experimental males. (*D*) Transit time of control *VillinCreERT2* and *VillinCreERT2;Neurog3*$^{fl/fl}$ animals. Statistical significance was determined by unpaired *t* test. n = 4 animals per genotype. (*E*) Jejunum of *VillinCreERT2* and *VillinCreERT2;Neurog3*$^{fl/fl}$ animals were harvested 6 days after initial tamoxifen treatment, separated into crypt (*circles*) and villus (*squares*) compartments, and analyzed for expression of enteroendocrine-specific genes by quantitative PCR. *Ngn3* (crypt, **$P = .001405$; villus, ****$P = .000029$), *Cck* (crypt, **$P = .007638$; villus, ****$P < .000001$), *Gip* (crypt, *$P = .02405$; villus, ****$P < .000001$), *Gcg* (crypt, **$P = .007729$; villus, **$P = .001133$), *Sst* (crypt, **$P = .008389$; villus, **$P = .001345$), and *Pyy* (crypt, $P = .071144$; villus, $P = .099997$). Statistical significance was determined using the Holm–Sidak method. n = 4–7 samples per compartment per genotype. (*F*) Serum levels of GIP and PYY 10 days after tamoxifen administration (GIP, $P = .0114$; PYY, *$P = .0141$). Statistical significance was determined using 1-way analysis of variance with the Tukey multiple comparison test. n = 5 mice per genotype. (*G*) Immunofluorescence staining for Chromogranin A (ChgA) in *VillinCreERT2;Neurog3*$^{fl/fl}$*;tdTomato* and *VillinCreERT2;tdTomato* control jejunum 6 days after tamoxifen administration. Ace2 marks the brush border. *Scale bars*: 100 mm. (*H*) tdTomato expression in the colon of control *VillinCreERT2;tdTomato* and *VillinCreERT2;Neurog3*$^{fl/fl}$*;tdTomato* animals 10 days after tamoxifen administration. Carbonic anhydrase 4 (CA4) marks the surface epithelial cells of colonocytes. *Scale bars*: 100 mm. (*I*) Quantification of the representative image shown in panel *F* (day 6, ****$P < .0001$; day 10, ****$P < .0001$; no difference between days 6 and 10). n = 6 mice per genotype per time point. Statistical significance was determined using 2-way analysis of variance with the Tukey multiple comparison test. (*J*) Total energy expenditure over time was measured by whole-body respirometry. *Arrows* indicate tamoxifen injections. n = 12 control, n = 14 EEC-deficient mice. ****$P < .0001$; statistical significance was determined using simple linear regression. (*K*) Total food eaten by control and EEC-deficient animals as measured by metabolic cages. n = 12 controls, n = 14 EEC-deficient mice. (*L*) Total activity performed by control and EEC-deficient animals as measured by metabolic cages. n = 12 controls, n = 14 EEC-deficient mice. GIP, glucose-dependent insulinotropic polypeptide; mRNA, messenger RNA; PYY, peptide YY.

into human intestinal organoids that contained all intestinal epithelial cell types and a supporting mesenchyme.[28] Organoids were transplanted into mice for an additional 12 weeks of growth. This resulted in intestinal tissues with robust crypt–villus architecture containing all mature cell types, including intestinal stem cells.[29] Similar to the murine model, EEC-deficient organoids displayed increased proliferation and expanded OLFM4+ stem and progenitor cells

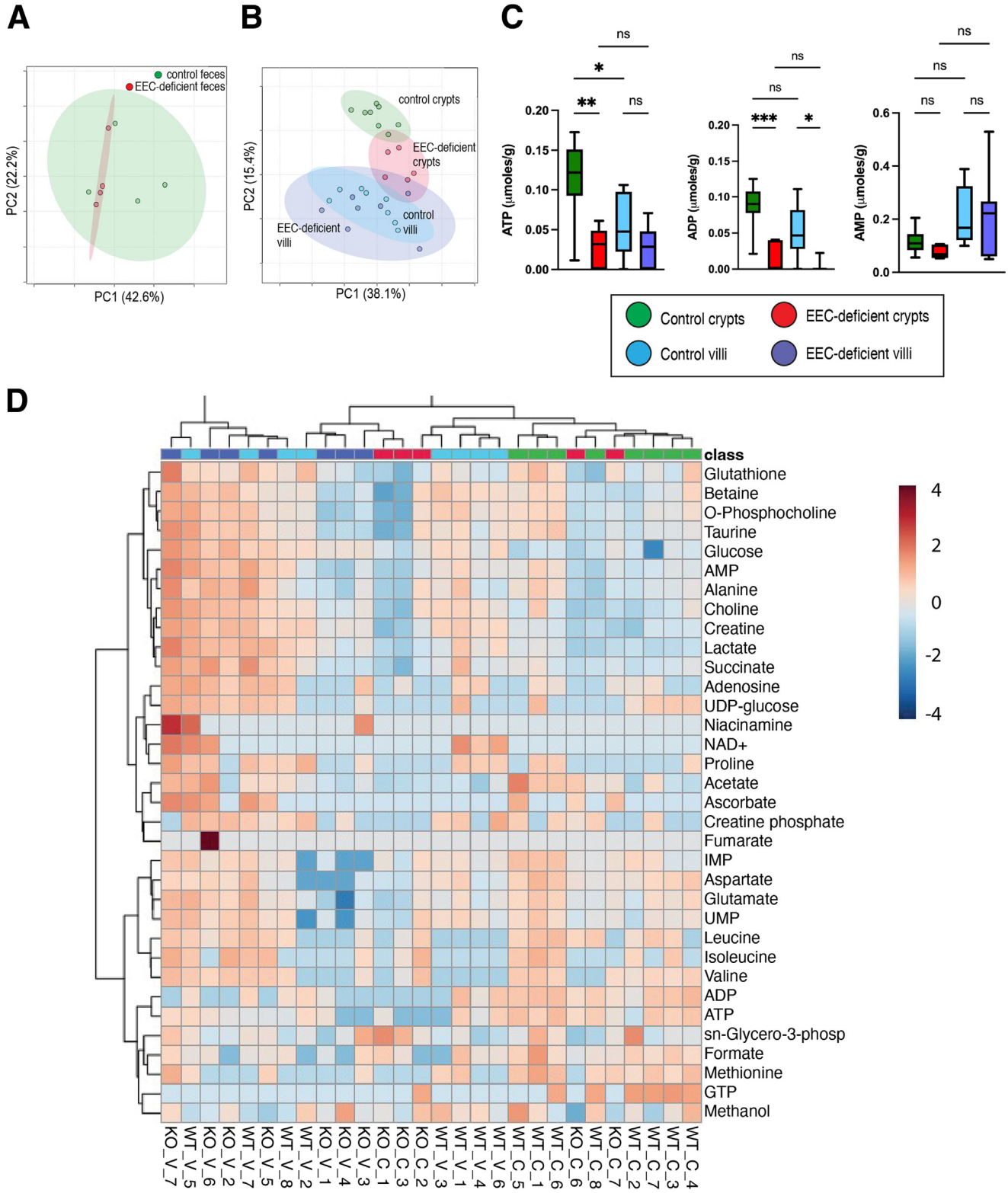

(Figure 4*H–J*). Moreover, crypts isolated from organoid transplants had increased enteroid-forming capacity compared with wild type (Figure 4*K*).

Crypts from EEC-deficient intestine had a phenotype resembling that of a nutrient-deficient environment even though animals were ingesting normal levels of food. From this, we hypothesized that EECs couple nutrient availability with crypt behaviors. Therefore, we predicted that if we eliminated the need for EECs to transmit the nutrient status to the crypt, ISC behavior would not be impacted by the absence of EECs. To do this, we grew crypts for multiple passages in culture in which intestinal stem cells consistently were exposed to nutrients in nutrient-rich media. Although EEC-deficient enteroids had a growth advantage immediately upon culture generation, which required splitting earlier than wild-type cultures, this difference normalized within 2 passages (Figure 4*L*). Expression of OLFM4 also normalized between genotypes over multiple passages. At passage 1, OLFM4 levels were approximately 12-fold higher in EEC-deficient enteroids (Figure 4*M*), but by passage 4 expression had increased to approximately 60-fold over passage 1 levels and largely had normalized between genotypes alongside the normalization in growth rate (Figure 4*N*). These data suggested that EECs are essential for relaying the nutrient status to the crypt in vivo when the crypt is restricted from direct access to nutritional cues, and that intestinal stem cells require input from the EEC to maintain homeostasis in vivo.

Without EECs, Intestinal Stem and Progenitor Cells Up-Regulate Lipid Metabolism Genes and Down-Regulate Master Nutrient Sensor mTOR Complex 1

To further investigate the mechanism by which EECs regulate metabolism in the intestinal crypt, we performed single-cell RNA (scRNA) sequencing of transplanted human intestinal organoids with and without EECs. After filtering and quality control of 3 wild-type organoids and 1 EEC-deficient organoid, 14,968 cells were recovered from the pooled wild-type samples and 4853 cells were recovered from the EEC-deficient sample. As previously described,[30] scRNA sequencing of wild-type organoids identified all the expected epithelial cell types, including intestinal stem cells, proliferative progenitors, Paneth-like cells, enterocytes, goblet cells, and EECs, whereas organoids generated from NEUROGENIN 3 (NEUROG3)-null pluripotent stem cells were specifically deficient in EECs (Figure 5*A* and *B*). We performed gene ontology analysis on the differentially expressed genes between wild-type and EEC-deficient organoids in multiple cell clusters. Strikingly, in the stem and progenitor cell clusters, we observed that all 20 of the top biological processes up-regulated in EEC-deficient organoids were associated with cellular metabolism, especially of lipids (Figure 5*C*). Lipid metabolism also was up-regulated in Paneth cells in EEC-deficient organoids (Figure 5*C*). Examples of genes involved in lipid metabolism that were up-regulated significantly in EEC-deficient crypt cells include *arylacetamide deacetylase (AADAC)*, *α ketoreductase family members 1C1 (AKR1C1)* and *1C3 (AKR1C3)*, *apolipoproteins A1 (APOA1)* and *A4 (APOA4)*, *catalase (CAT)*, *fatty acid binding protein 2 (FABP2)*, and *microsomal triglyceride transfer protein (MTTP)* (Figure 5*D*). These human data are consistent with the functional data obtained in mice, and together all data suggest that loss of EECs results in up-regulation of fatty acid oxidation and a deficit of nutrient sensing in the crypts.

As a final investigation of how crypts from EEC-deficient small intestine might be impaired in their ability to sense nutrients, we analyzed activity of the master cellular pathway governing nutrient sensing, mammalian target of rapamycin (mTOR). In response to abundant nutrients, mTOR complex 1 (mTORC1) signaling, as measured by the phosphorylation of downstream target S6 kinase (phospho-S6), activates an array of downstream catabolic pathways. In fasted animals, when nutrients are low, mTORC1 signaling is decreased in the crypt.[19] Similar to the fasted state, crypts in EEC-deficient mice and human intestinal organoids show a marked reduction of phospho-S6 in the crypts compared with fed control animals (Figure 6*A* and *B*). We observed high levels of phospho-S6 in Paneth cells of fed control animals, as previously described,[19] while largely being excluded from Leucine-rich repeat-containing G protein-coupled receptor 5 (Lgr5+) stem cells (Figure 6*C* and *D*), suggesting discrete cellular metabolic programs that may undergo regulation by EECs. Together, our data suggest that EECs are required to transmit nutritional information to activate the nutrient-sensing, master metabolic regulator mTORC1 in Paneth cells in the crypt, and are required to restrict a fatty acid metabolic program in intestinal stem and progenitor cells (Figure 6*E*).

Discussion

In this study, we identified that enteroendocrines regulate crypt metabolism and intestinal stem cell homeostasis. By using mice and human pluripotent stem cell–derived intestinal organoids, we found that EECs are essential for

Figure 2. (***See previous page***). **EECs are required to maintain intestinal metabolism along the crypt–villus axis.** (*A*) Principal component (PC) analysis score plot of ^{1}H-NMR metabolomics data, PC1 (42.6% expected value (EV)) and PC2 (22.2% EV), indicating no significant difference in metabolic profiles in feces isolated from control and EEC-deficient animals. Green, control animals (n = 4); red, EEC-deficient animals (n = 4). (*B*) PCA score plot of ^{1}H-NMR metabolomics data, PC1 (38.1% EV) and PC2 (15.4% EV), indicating the presence of unique metabolic profiles in crypts and villi from control and EEC-deficient animals. Green, control crypt (n = 8); red, EEC-deficient crypt (n = 5); light blue, control villi (n = 8); and purple, EEC-deficient villi (n = 7). (*C*) Normalized concentrations of ATP and ADP per gram of tissue. Significance was calculated by 1-way analysis of variance with the Tukey multiple comparison test. ATP, $^{*}P = .0231$, $^{**}P = .0029$, $^{**}P = .0019$; and ADP, $^{*}P = .0113$, $^{***}P = .0006$, $^{****}P < .00001$. (*D*) Ward Euclidean hierarchical clustering heatmap depicting the 34 metabolites identified by ^{1}H-NMR metabolomics across the control and EEC-deficient crypt (C) and villus (V) samples. AMP, adenosine monophosphate; ADP, adenosine diphosphate; ATP, adenosine triphosphate; GTP, guanine triphosplate; IMP, inosine monophosphate; NAD, nicotinamide adenine dinucleotide; UDP, uridine diphosphate; UMP, uridine monophosphate.

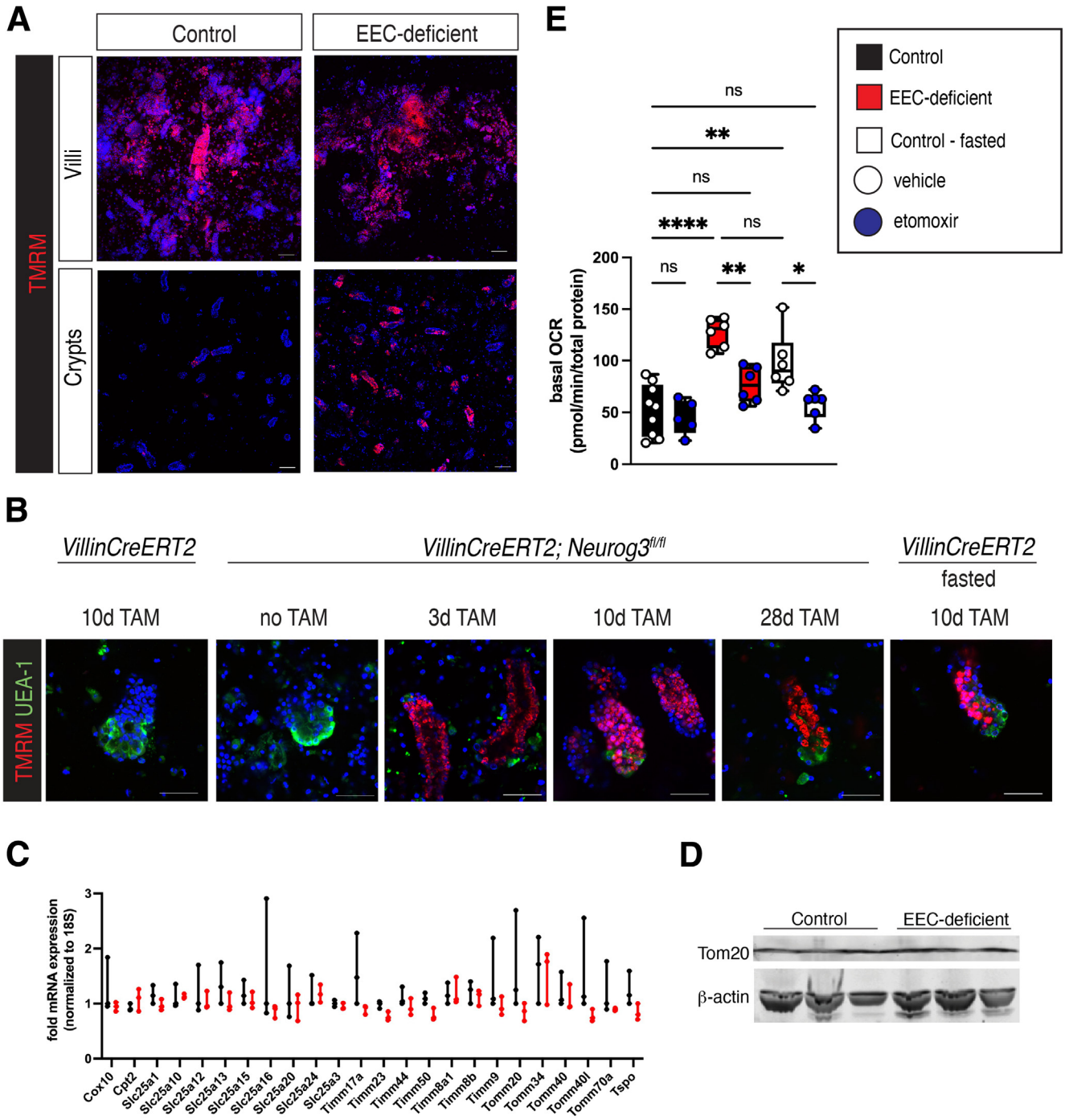

Figure 3. EECs regulate mitochondrial activity in intestinal crypts. (*A*) Crypts and villi were separated from jejunum of control and EEC-deficient animals and incubated in TMRM and Hoechst to visualize active mitochondria via live confocal microscopy. *Scale bars*: 10 mm. Images shown are representative of 11 experiments. (*B*) High magnification of crypts from representative control mice, *VillinCreERT2;Neurog3*$^{fl/fl}$ mice without tamoxifen (n = 2), 3 days after tamoxifen (n = 2), 10 days after tamoxifen (n = 11), 28 days after tamoxifen (n = 2), and control mice after a 16-hour overnight fast (n = 4). Paneth cells are labeled with *Ulex europaeus* Agglutinin 1 (UEA-1). *Scale bars*: 50 mm. (*C*) TaqMan array for genes encoding inner- and outer-mitochondrial membrane proteins in control and EEC-deficient crypts. n = 3 animals per genotype. (*D*) Crypt cells were probed for mitochondrial membrane protein Tom20 by Western blot. β-actin was used as a loading control. n = 3 animals per genotype. (*E*) Crypts of control and EEC-deficient animals were plated for Seahorse analysis of mitochondrial activity. Basal oxygen consumption of control and EEC-deficient crypts, with and without the fatty acid oxidation inhibitor etomoxir (****P = .00001, control vs EEC-deficient; *P = .018, control vs control-fasted; and **P = .005, EEC-deficient v EEC-deficient + etomoxir). Statistics calculated using 1-way analysis of variance with the Tukey multiple comparison test. Error bars represent the SEM. Each experiment was conducted on at least 7 replicates of 500 crypts per well. N = 5–9 experiments per condition. mRNA, messenger RNA; TAM, tamoxifen.

restricting mitochondrial metabolism and controlling intestinal stem cell activity. In the absence of EECs, intestinal crypts adopt fasting-like characteristics, including increased mitochondrial activity, activation of fatty acid oxidation, increased intestinal stem cell activity, and reduction of activity of the master nutrient-sensing mTORC1 pathway. Although some EEC-derived peptides, such as glucagon-like peptide 2 (GLP-2)[31,32] and neurotensin,[33] have established roles in nutrient-sensitive mucosal growth and intestinal stem cell function, this study links EECs with the regulation of crypt metabolism, a key regulator of intestinal homeostasis. Because the frequency of different EEC peptides varies along the proximal–distal axis of the gastrointestinal tract, we hypothesize that specific hormonal regulatory mechanisms in the proximal small intestine may differ from those in the ileum and colon. This correlates with changes in the luminal cues sensed and transmitted from EECs to the underlying crypts.

We found that loss of EECs results in an altered metabolic environment in all cells residing in the crypt, including intestinal stem cells, proliferative progenitor cells, and Paneth cells. Paneth cells are important niche cells contributing metabolites and growth factors to the intestinal stem cell to maintain stemness and function[2] and maintain an independent metabolic identity from intestinal stem cells.[13] Moreover, mTORC1 signaling is known to be high in Paneth cells and acts as a key regulatory pathway coupling nutrient providing availability to intestinal stem cell function.[19] Under normal conditions, Paneth cells mainly use glycolysis; however, in EEC-deficient human intestinal organoids, we observed increased expression of lipid metabolism genes. This shift from glycolysis to lipid metabolism correlated with reduced mTORC1 signaling in human and mouse Paneth cells. These disruptions in Paneth cell metabolism raise the possibility that EECs may lie upstream of Paneth cells in regulating niche homeostasis. In addition, our data suggest that EECs could act on intestinal stem cell metabolism independently of Paneth cells, providing another environmental input in the maintenance of homeostasis.

EECs secrete more than 20 distinct biologically active peptides and other small molecules, such as ATP, in response to environmental stimuli[3] such as luminal nutrients and microbial metabolites. In this study, we depleted EECs from adult animals and found no short-term changes in body weight, amount of food consumed, fecal output, microbial metabolites, or villus epithelial metabolites compared with control animals. These data suggest that, over the 10-day time course studied in these experiments, there were minimal changes in the ability of the intestinal epithelium to adequately absorb nutrients. However, because crypt metabolism and function in EEC-deficient animals phenocopied fasted animals, we concluded that the ability of the intestinal epithelium to sense the presence of luminal nutrients was disrupted. The identity of the environmental stimuli that trigger release of EEC products to affect intestinal metabolism and homeostasis remain unknown.

EEC regulation of intestinal metabolism has implications for numerous gastrointestinal pathologies, including colorectal cancer, gastric cancer, and inflammatory bowel disease (IBD). EEC number and hormone production are altered in diseases such as IBD and type 2 diabetes. EECs are increased overall in mouse models of colitis and human patients with ulcerative colitis and Crohn's disease, although the populations of hormones are skewed in each disease.[34] In ulcerative colitis, there was a significant increase in serotonin, but no change in peptide YY, pancreatic polypeptide, GLP-1, or somatostatin-expressing cells. Conversely, in patients with Crohn's disease, there was a similar significant increase in serotonin-expressing cells, increased GLP-1, no change in somatostatin, and loss of peptide YY and pancreatic polypeptide compared with healthy controls. Although there have been limited reports of EEC activity in human patients with colorectal cancer, there have been some in vitro studies reported. In colon cancer cell lines, ghrelin[35,36] stimulated proliferation and metastatic potential, whereas activation of the GLP-1 receptor inhibited cell growth and induced apoptosis in tumor-bearing mice.[37] Moreover, the shift in cellular metabolism in response to changing nutrient availability within the tumor environment[38] suggests potential roles for multiple nutrient-sensing EECs in tumor proliferation and pathogenesis.

Numerous diseases are associated with changes in cellular metabolism. Most cancers alter their cellular metabolism to consume high levels of glucose and produce ATP rapidly via aerobic glycolysis, termed the *Warburg effect*. In addition, a number of other metabolic pathways, including glutamine, lipid, oxidative phosphorylation, and 1-carbon metabolism, all can be dysregulated in cancer, including colorectal cancer.[38] Mitochondrial dysfunction is a hallmark of IBD, partially attributed to genetic susceptibility factors and largely owing to the microbial–epithelial environment of the gut epithelium itself.[8] In Crohn's disease and ulcerative colitis, many studies have shown diminished mitochondrial energy production, an increase in reactive oxygen species, an increase in cell stress, and diminished autophagy—all driving an inflammatory disease process.[8] The pathologic changes in the intestine after loss of EECs are relevant to several disease contexts. For example, one of the most highly up-regulated genes we identified in Paneth cells from human intestinal organoids that lacked EECs was *catalase*, an antioxidant enzyme that protects cells from oxidative stress. In addition, gene ontology analysis suggested that Paneth cells from EEC-deficient organoids may have altered metal ion processing, including that of zinc, copper, and chromate. These metals can be oxidized to produce free radicals and contribute to reactive oxygen species–induced stress throughout the body, and are pathogenic contributors to gastrointestinal cancers and IBD.[39] Our data suggest that EECs may serve an as yet unidentified role in protecting Paneth cells from oxidative stress.

In moving forward, it will be important to determine how EECs integrate particular nutritional or microbial cues with specific secreted products to integrate luminal inputs with metabolic pathways and functional outcomes. With this information, it should be possible to develop practical new therapeutic avenues for

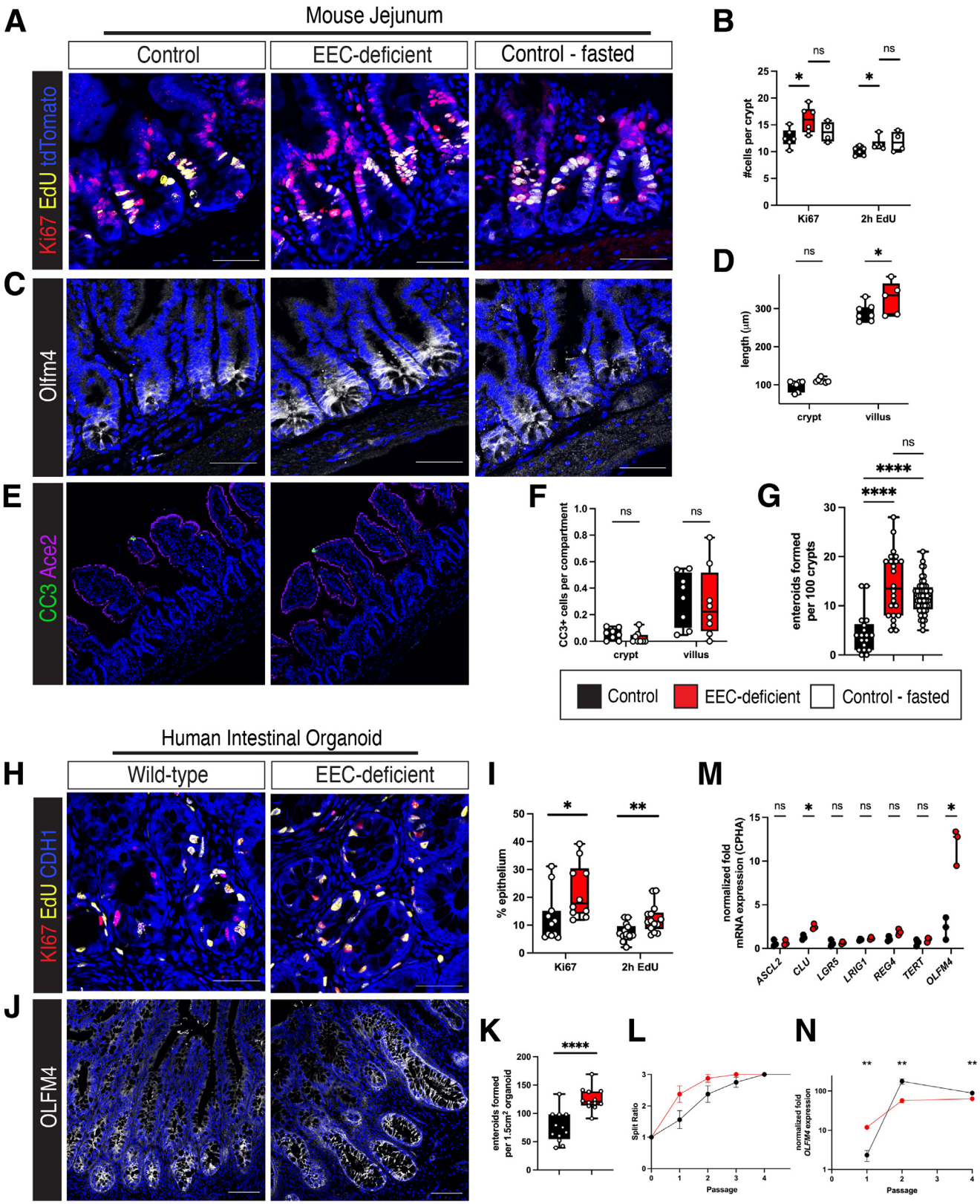

patients with metabolic disease, IBD, or gastrointestinal cancers.

Materials and Methods

Mice

B6.Cg-Tg(Vil1-cre/ERT2)23Syr/J[22] (#020282; JAX), B6.Cg-*Gt(ROSA)26Sor*$^{tm9(CAG\text{-}tdTomato)Hze}$/J[24] (#007909, Ai9; JAX), and *Neurog3*$^{fl/fl}$[6] were maintained on a C56Bl/6 background. B6.129P2-*Lgr5*$^{tm1(cre/ERT2)Cle}$/J (#008875; JAX) were on a mixed background. At 8–12 weeks of age, animals were administered 2 doses of tamoxifen (25 mg/kg), dissolved in corn oil, 3 days apart. For all experiments, controls were *VillinCreERT2;Neurog3*$^{+/+}$ animals administered tamoxifen following the same protocol as *VillinCreERT2;Neurog3*$^{fl/fl}$ mice. Mice with and without the tdTomato reporter were used interchangeably. Animals were housed in a specific pathogen–free barrier facility in accordance with National Institutes of Health Guidelines for the Care and Use of Laboratory Animals. All experiments were approved by the Cincinnati Children's Hospital Research Foundation Institutional Animal Care and Use Committee (2022-0002) and performed using standard procedures. Mice were maintained on a 12-hour light/dark cycle and had ad libitum access to standard chow and water. Mice were housed at 22ºC at 30%–70% humidity.

Diarrhea Score

The abdomen was opened and visually inspected for the consistency of intestinal contents. Animals were scored based on luminal distension and the liquidity of luminal contents in the small intestine, cecum, and proximal colon. Animals were given a score of 0 for no liquid contents and well-defined stool pellets forming along the colon; a score of 1 for no liquid contents and poorly defined stool pellets merging together in the colon; a score of 2 for mild distension, some liquid contents in the small intestine and/or cecum, and poorly defined stool pellets merging together in the colon; a score of 3 for severe distension, watery luminal contents in the small intestine and/or cecum, and poorly defined stool pellets merged together in the proximal colon.

Transit Time

Mice that were eating chow ad libitum were orally gavaged with 100 mL water dyed with blue food coloring (Kroger). Thirty minutes later, the animal was killed and the entire gastrointestinal tract was removed and measured. The distance the dye-front had traveled was expressed as a percentage of the length of the small intestine as previously described.[7]

Serum Hormone Levels

Hormone concentrations in the mouse serum were determined using Milliplex Mouse Metabolic Hormone Expanded Panel–Metabolism Multiplex Assay (#MMHE-44K; MilliporeSigma) according to the manufacturer's protocol.

Indirect Calorimetry

Eight- to 12-week-old male mice were moved from standard housing to metabolic cages (Promethion; Sable Systems International) for 14 days according to standard protocol. Mice were acclimatized for 3 days before administration of the first dose of tamoxifen. Mice were continuously recorded at ambient room temperature (22°C) on a

Figure 4. (*See previous page*). EECs regulate intestinal stem cell and progenitor activity. (*A*) Immunofluorescence staining for Ki67 and 5-ethynyl-2'-deoxyuridine (EdU) (2-hour pulse) in control, EEC-deficient, and fasted control mouse jejunal crypts. 4′,6-Diamidino-2-phenylindole (DAPI) counterstains nuclei in blue. *Scale bars*: 50 mm. (*B*) Quantification of proliferation in panel *A*. **P* = .02, Ki67; **P* = .04, EdU. Statistics were calculated using an unpaired *t* test with the 2-stage step-up (Benjamini, Krieger, and Yekutiele method). N = 6 mice per genotype. (*C*) Immunofluorescence staining for Olfactomedin-4 (Olfm4) in control, EEC-deficient, and fasted control mouse jejunal crypts. DAPI counterstained nuclei is shown in blue. *Scale bars*: 50 mm. Representative images shown from 6 mice per genotype. (*D*) Quantification of crypt depth and villus height in control and EEC-deficient jejunum. Statistics were calculated by 2-way analysis of variance with the Sidak multiple comparison test. **P* = .028. n = 7 animals per genotype. (*E*) Immunofluorescence staining for cleaved caspase-3 (CC3) in control and EEC-deficient small intestine. Angiotensin converting enzyme 2 (Ace2) marks the brush border and DAPI counterstained nuclei. *Scale bars*: 50 mm. Representative image of 8 mice per genotype. (*F*) Quantification of panel *E*. Three well-oriented images per mouse were averaged and the number of cleaved caspase-3–positive cells per number of crypts and villi per image is represented. n = 8 mice per genotype. (*G*) Enteroid forming capacity of control, EEC-deficient, and fasted control mouse jejunal crypts (*****P* < .0001). n = 18 wells from 3 control mice, 24 wells from 4 EEC-deficient mice, and 48 wells from 4 fasted control mice. Statistics were calculated using ordinary 1-way analysis of variance with the Tukey multiple comparison test. (*H*) Immunofluorescence staining for Ki67 and EdU (2-hour pulse) in wild-type and EEC-deficient human intestinal organoids (HIO). DAPI counterstained nuclei in blue. *Scale bars*: 50 mm. (*I*) Quantification of proliferation in panel *H*. **P* = .032, Ki67; ***P* = .007, EdU. Statistics were calculated using an unpaired *t* test with the Holm–Sidak method. N = 11–14 organoids. (*J*) Immunofluorescence staining for OLFM4 in wild-type and EEC-deficient human intestinal organoids. DAPI counterstained nuclei in blue. *Scale bars*: 20 mm. Representative images shown from 5 organoids per genotype. (*K*) Enteroid forming capacity of wild-type and EEC-deficient human intestinal organoid crypts (*****P* < .0001). n = 12 wells from 2 independent organoids per genotype. Statistics were calculated using an unpaired 2-tailed *t* test. (*L*) Visualization of HIO-derived enteroid growth as depicted by split ratios at each passage. The slope of the curves was significantly (**P* = .03) different from passage 0 to passage 2. Statistical significance was determined by simple linear regression. n = 3–4 independent enteroid lines per genotype. (*M*) Normalized (to cyclophilin, CPHA) messenger RNA (mRNA) expression for a selection of intestinal stem cell genes at first passage of enteroids derived from wild-type and EEC-deficient human intestinal organoids. Statistics were calculated by an unpaired 2-tailed *t* test. n = 3 independent enteroid lines per genotype. (*N*) Quantitative PCR (qPCR) depicting normalized mRNA expression for *OLFM4* in HIO-derived enteroids collected at passages 1, 2, and 4. Statistics were calculated by an unpaired 2-tailed *t* test. n = 3–4 independent enteroid lines per genotype.

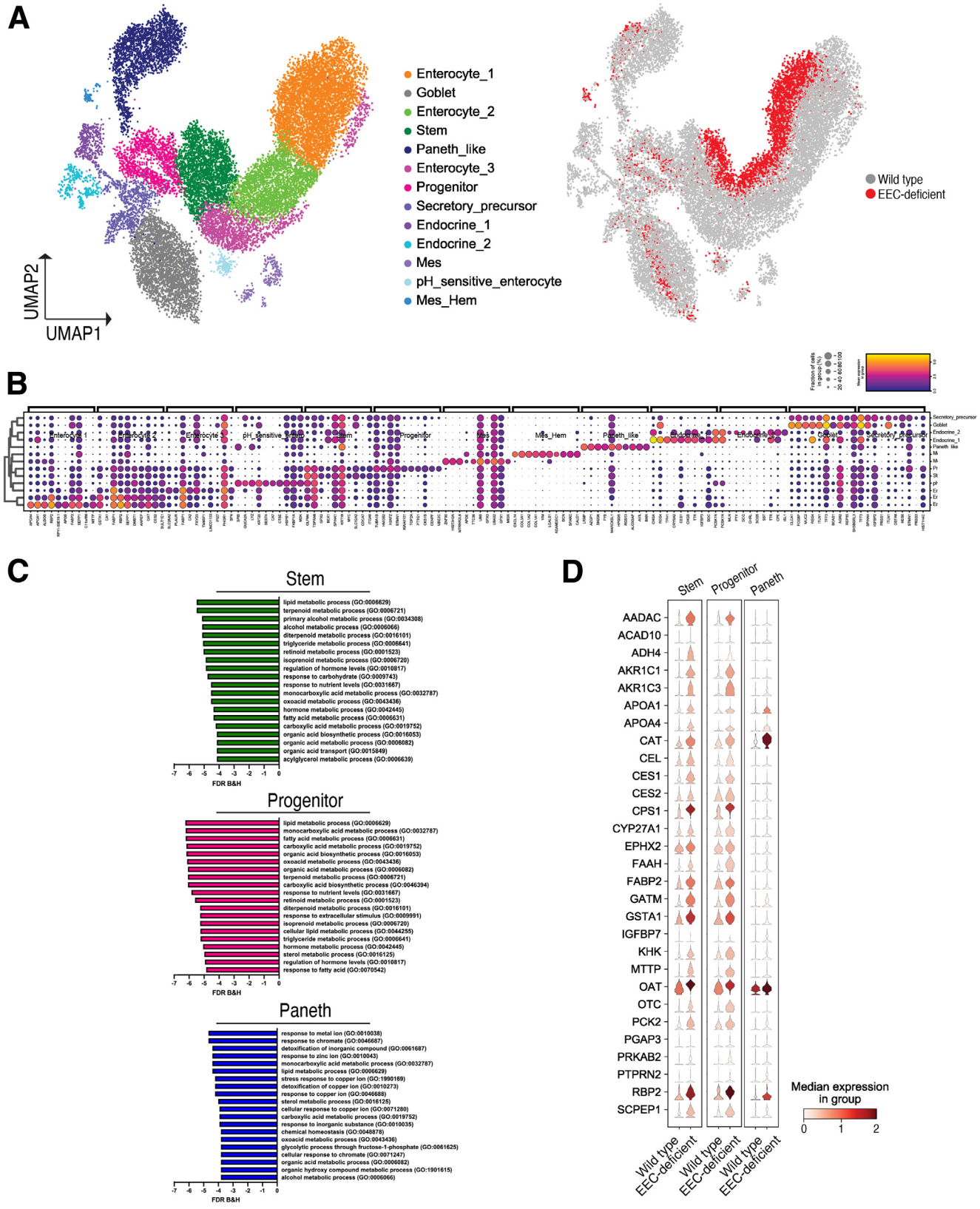

Figure 5. Without EECs, intestinal stem and progenitor cells up-regulate lipid metabolism genes. (*A*) Transplanted human intestinal organoids were dissociated into single cells and sequenced using the 10x Genomics platform (n = 3 wild-type, n = 1 EEC-deficient). Uniform manifold approximation and projection (UMAP) depicting the integrated data set of all cells colored by cluster (*left*) and colored by genotype (*right*). (*B*) Dot plot depicting the expression of the top 10 genes in each cell cluster in the integrated data set. (*C*) Gene Ontology analysis of the differentially expressed genes in EEC-deficient stem (*top*, green), progenitor (*middle*, pink), and Paneth-like (*bottom*, blue) cell clusters. The top 20 biological processes are displayed. (*D*) Violin plots for a selection of genes represented in GO:0006629, lipid metabolic process, in the stem, progenitor, and Paneth-like cell clusters in wild-type and EEC-deficient human intestinal organoids. B&H, Benjamini and Hochberg; FDR, false discovery rate.

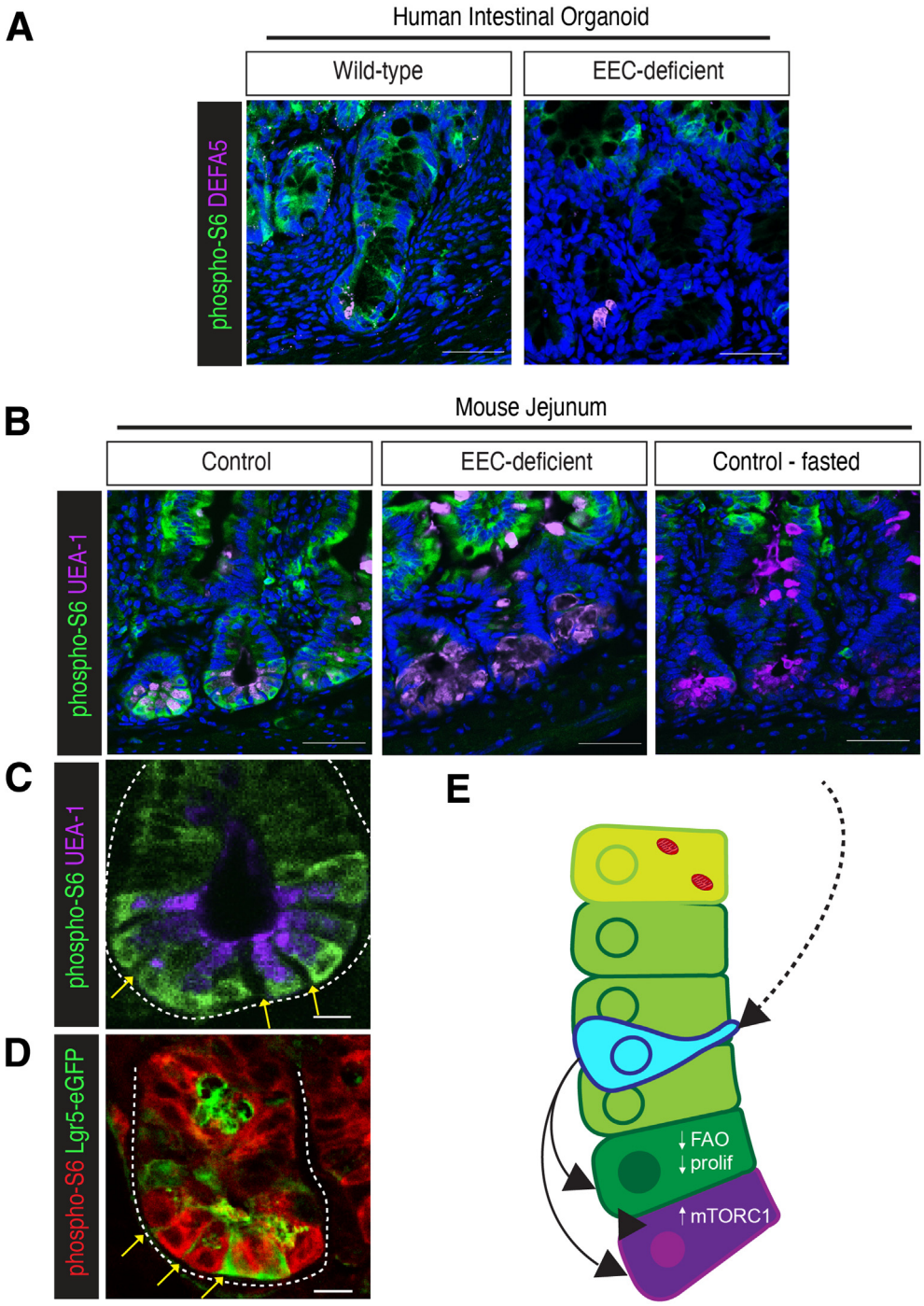

Figure 6. Without EECs, intestinal stem and progenitor cells down-regulate master nutrient sensor mTORC1 in Paneth cells. (*A*) Immunofluorescence staining for phospho-S6 in crypts of wild-type and EEC-deficient human intestinal organoids. Defensin A5 (DEFA5) marks Paneth cells. 4′,6-Diamidino-2-phenylindole (DAPI) counterstained nuclei in blue. *Scale bar*: 50 mm. Representative image of 5 organoids per genotype. (*B*) Immunofluorescence staining for phospho-S6 in small intestinal crypts of control, EEC-deficient, and fasted control mice. *Ulex europaeus* Agglutinin 1 (UEA-1) marks Paneth cells. DAPI counterstained nuclei in blue. *Scale bar*: 50 mm. Representative image of 6 control, 6 EEC-deficient, and 3 fasted control mice. (*C*) Higher magnification of crypt of control mouse in panel *B*. *Arrows* point to areas negative for phospho-S6 staining between Paneth cells. (*D*) Immunofluorescence staining for phospho-S6 in small intestinal crypts of *Lgr5-eGFP-CreERT2* reporter mice. *Arrows* point to (eGFP)+ crypt–base columnar cells negative for phospho-S6 staining. *Scale bar*: 10 mm. Representative image of 3 mice. (*E*) Model depicting EEC regulation of crypt homeostasis and metabolism in response to nutrients (*dashed arrow*). In the fed condition, EECs (blue) activate mTORC1 signaling in Paneth cells (purple) and restrict intestinal stem cell activity, proliferation, and fatty acid oxidation (FAO) (dark green) (solid arrows). As progenitors (light green) move toward the villus and differentiate into absorptive enterocytes (light yellow), mitochondria undergoing FAO become abundant. eGFP, enhanced green fluorescent protein; prolif, proliferation.

14-hour light: 10-hour dark (14L:10D) light cycle with the following measurements taken every 5 minutes using Sable Systems International acquisition software (Promethion Live v.21.0.3): oxygen consumption (Vo_2), carbon dioxide emission (VCO_2), energy expenditure, respiratory exchange ratio, food intake, water intake, and spontaneous locomotor activity (cm s^{-1}) in the XY plane. Food and water were available ad libitum. Energy expenditure was calculated using the abbreviated Weir formula. The respiratory exchange ratio was calculated by the ratio VCO_2/VO_2. Mass-dependent variables (VO_2, VCO_2, energy expenditure) were not normalized to body weight. Food and water intake were measured by top-fixed load cell sensors, from which food and water containers were suspended into the sealed cage environment. Raw data were exported using Sable Systems International ExpeData software v.1.9.27 and analyzed using Sable Systems International MacroInterpreter Software v.2.43. Reported data represent a combination of 2 independent experiments conducted separately.

Crypt/Villus Separation

The small intestine was flushed with ice-cold phosphate-buffered saline (PBS) without Mg^{2+} or Cl^{2+} (#10010-049; Gibco) or with Dulbecco's modified Eagle medium (#12634028; Gibco) containing 10% fetal bovine serum (FBS) (#12306C; Sigma-Aldrich) and divided into duodenum, jejunum, and ileum. The jejunum was filleted open and rinsed vigorously to remove mucus and debris, then cut into 1- to 2-cm segments and transferred to a 15-mL conical containing 5 mL 200 mmol/L EDTA (#15575020; Invitrogen) in PBS without Mg^{2+} or Cl^{2+}. Tissue segments were shaken vigorously by hand for 30 seconds and then rotated for 30 minutes at 4ºC. Tissue segments then were transferred to a new 15-mL conical containing 5 mL of 1.5% sucrose and 1% sorbitol in PBS without Mg^{2+} or Cl^{2+} and shaken by hand for 2 minutes at a rate of 2 shakes per second to dislodge crypts. The solution containing crypts and villi then was filtered through a 70-um filter set atop a 50-mL conical tube, with crypts enriched in the filtered fraction. Villi were collected by washing the top of the filter with additional PBS without Mg^{2+} or Cl^{2+} and recovering the unfiltered fraction into a new conical tube. All steps were performed on ice. Crypts and villi were inspected via microscopy and then centrifuged at 150 × *g* for 10 minutes at 4ºC before additional assays.

Immunofluorescence

Mouse intestine and human intestinal organoids were fixed in 4% paraformaldehyde, cryopreserved in 30% sucrose, embedded in Optimal Cutting Temperature compound (OCT) (Sakura Finetek), and frozen at -80ºC until they were cryosectioned. Eight-mm cryosections were mounted on Superfrost Plus slides (Fisher) and permeabilized, blocked, and stained according to standard protocol. The primary antibodies used are listed in Table 1. All secondary antibodies were conjugated to Alexa Fluor 488, 546/555/568 or 647 (Invitrogen) and used at 1:500 dilution. 5-ethynyl-2'-deoxyuridine (EdU) was retrieved and stained using the Click-It EdU Alexa Flour 647 Imaging Kit (#C10340; Invitrogen). Images were acquired using a Nikon A1 GaAsP LUNV inverted confocal microscope and NIS Elements software (Nikon). For images used for quantification, at least three 20× images were taken with well-oriented crypt–villus architecture and the average counts from the 3 images are represented. On average, 30–40 crypts per animal were counted.

Quantitative Polymerase Chain Reaction

RNA was extracted using the Nucleospin RNA extraction kit (#740955; Macherey-Nagel) and reverse-transcribed into complementary DNA using Superscript VILO (#11-754-250; Invitrogen) according to the manufacturer's instructions. Quantitative polymerase chain reaction (PCR) was performed using the Quantitect SYBR Green PCR kit (#204145; QIAGEN). For mitochondrial genes, a custom TaqMan array preloaded with the mouse mitochondrial panel (Applied Biosystems) was used with TaqMan Fast Advanced Master mix. SYBR Green and TaqMan quantitative PCR were run on a QuantStudio 3 Flex Real-Time PCR System (Applied Biosystems). Relative expression was determined using the delta delta Ct method and normalizing to 18S (mouse) or cyclophilin (CPHA) (human). The primers used are listed in Table 2.

Human Intestinal Organoids

Wild-type (H1) and EEC-deficient (NEUROG3$^{-/-}$) human pluripotent stem cells[40,41] were maintained, differentiated into intestinal organoids, and transplanted into the kidney capsule of immunocompromised NOD.Cg-*Prkdc*^{scid} *Il2rg*^{tm1Wjl}/SzJ mice (#005557; JAX) as previously described.[7,42] Organoids were harvested after 10–14 weeks of growth. Organoids were opened and washed to remove mucus, dead cells, and cellular debris from the lumen, then equally sized approximately 1.5-cm^2 segments containing well-developed crypt–villus architecture were placed in a 15-mL conical tube containing 5 mL TryPLE Dissociation Reagent (#12563029; GIBCO) for 30 minutes, shaking at 4ºC. Organoids were shaken vigorously to dislodge villi and then moved to a Sylgard-coated dish (Dow Chemical) where crypts were scraped from the serosal tissue using the back of curved forceps. Crypts and villi were inspected via microscopy and then centrifuged at 150 × *g* for 10 minutes at 4ºC before additional assays.

TMRM

Crypt and villus fractions were suspended in Live Cell Imaging Solution (#A14291DJ; Invitrogen) containing 100 nmol/L TMRM (#T668; Invitrogen), 10 ug/mL Hoescht (#H3570; Thermo Scientific), and *Ulex europaeus* Agglutinin 1 conjugated to DyLight 649 (Vector Laboratories) or fluorescein (Invitrogen), both at 1:1000 dilution. Samples were incubated for 30 minutes at 37ºC, washed with PBS, centrifuged at 150 × *g* for 5 minutes, resuspended in phenol red–free, growth-factor–reduced basement-membrane Matrigel (#356231; Corning), and plated on glass-bottom dishes for confocal live imaging. Once the Matrigel had solidified, Live Cell Imaging Solution was overlaid on the samples. Images were acquired using a Nikon A1 GaAsP LUNV inverted confocal microscope and NIS Elements

Table 1. Antibodies Used for Immunofluorescence Staining

Antibody	Company	Catalog #	Host	Dilution
Angiotensin Converting Enzyme 2 (Ace2)	R&D Systems	AF3437	Goat	1:200
Chromogranin A	ImmunoStar	20085	Rabbit	1:200
Carbonic anhydrase 4	R&D Systems	AF2414	Goat	1:200
Ki67	Cell Marque	275R-14	Rabbit	1:200
Cleaved caspase-3	Cell Signaling Technology	9661S	Rabbit	1:200
Defensin A5 (DEFA5)	Novus Biologicals	NB110-60002	Mouse	1:60,000
Green Fluorescent Protein (GFP)	Aves Labs	GFP-1020	Chicken	1:200
Olfm4 (mouse specific)	Cell Signaling Technology	39141S	Rabbit	1:200
OLFM4	Cell Signaling Technology	14369T	Rabbit	1:200
Phospho-S6 ribosomal protein (S235/236)	Cell Signaling Technology	2211S	Rabbit	1:200
UEA-1, DyLight 649	Vector Laboratories	DL-1068	N/A	1:1000
UEA-1, fluorescein	Invitrogen	L32476	N/A	1:1000

UEA-1, *Ulex europaeus* Agglutinin 1.

software (Nikon). Laser power was set based on TMRM intensity in wild-type villus samples and not adjusted between samples.

Seahorse

Mouse jejunal crypts were analyzed using the Seahorse XF96e bioanalyzer (Agilent Technologies) according to the manufacturer's instructions and according to protocols adapted from others.[43,44] The day before the assay, the 96-well plate was coated with basement membrane Matrigel (Corning) diluted 1:10 in complete Seahorse medium and set overnight at room temperature. The day of the assay, the coated plate was incubated in a non-CO_2 incubator at 37°C for 2 hours before plating crypts. Five hundred crypts per well were plated in complete Seahorse medium and allowed to attach for 1 hour at 37°C in a non-CO_2 incubator before analysis. Some wells were injected with etomoxir (4 mmol/L final concentration). After the experiment was completed, total protein was calculated using a Pierce BCA protein assay (#23227; Thermo Scientific) and all values were normalized to total protein.

Enteroid Formation Assay

Mouse jejunal crypts were plated at a density of 100 crypts per well in a 24-well plate in phenol red–free, growth factor–reduced basement membrane Matrigel (#356231; Corning) and fed with enteroid growth media containing 50% Wnt3a, R-spondin 3 and Noggin (L-WRN) conditioned media.[45] Seventy-two hours after plating, the number of spherical enteroids growing in each well was counted.

Human intestinal organoids were dissociated as described earlier. The villus fraction was discarded. Crypts

Table 2. Primers Used for qPCR.

Target	Species	Forward primer	Reverse primer
18S	Mouse	CTGAACGCCACTTGTCCCTC	GGCCGTTCTTAGTTGGTGGAGCG
Neurogenin3	Mouse	AGGTTGTTGTGTCTCTGGGG	GTCACTGACTGACCTGCTGC
Cholecystokinin (Cck)	Mouse	TTATTCTATGGCTGGGGTCC	ACTGCTAGCGCGATACATCC
Glucose-dependent insulinotropic polypeptide (Gip)	Mouse	TTGTCCTCCTTTCCCTGAGA	CAGAGGGGGAAGAAGAGTGA
Glucagon (Gcg)	Mouse	TGCCTTGCACCAGCATTAT	TGTCTACACCTGTTCGCAGC
Somatistatin (Sst)	Mouse	TTCTCTGTCTGGTTGGGCTC	CAGACTCCGTCAGTTTCTGC
Peptide YY (Pyy)	Mouse	CAGGATTAGCAGCATTGCGA	CCTCCTGCTCATCTTGCTTC
Cyclophilin (CPHA)	Human	CCCACCGTGTTCTTCGACATT	GGACCCGTATGCTTTAGGATGA
Achaete-Scute family BHLH transcription factor 2 (ASCL2)	Human	CACACAGGCTTCTCCCTAGC	CAAGATCTGGACACGAGCAG
Clusterin (CLU)	Human	CCCACACTTCTGACTCGGAC	CCCGTAGGTGCAAAAGCAAC
Leucine-rich repeat-containing G protein coupled receptor 5 (LGR5)	Human	TGGGAATGTATGTCAGAGCG	CAGCGTCTTCACCTCCTACC
Leucine-rich and Immunoglobulin-like domains 1 (LRIG1)	Human	CTGAACGCCTGTCTTCCAGG	CCGATTCGGGCAAGGTGTA
Regenerting Family Member 4 (REG4)	Human	TGGTTGCCAAACAGAATGCC	CACTCGCCCCTGTTAGCTTC
(Telomerase Reverse Transcriptase (TERT)	Human	GAGAACAAGCTGTTTGCGGG	AAGTTCACCACGCAGCCATA
Olfactomedin-4 (OLFM4)	Human	TCAGCAAACCGTCTGTGGTT	TCCCTACCCCAAGCACCATA

were split equally into 6 wells in a 24-well plate in phenol red–free, growth factor–reduced basement membrane Matrigel (#356231; Corning) and fed with human IntestiCult Organoid Growth Media (#06010; STEMCELL Technologies). Ninety-six hours after plating, the number of spherical enteroids growing in each well was counted.

NMR

Fecal samples were lyophilized for 2 days and weighed into 2-mL tubes containing 2.8 mm ceramic beads before processing. A total of 0.7 mL cold PBS was added to the dried fecal sample and the samples were homogenized for 2 cycles of 30 seconds at 5000 rpm using Precellys Evolution (Bertin Technologies). Upon centrifugation, supernatants were filtered at 10,000 $\times$ g for 120 minutes at 4ºC using prewashed 3-kilodalton spin filters. The NMR buffer was added to 500 μL fecal filtrate up to 600 μL, which contains the 0.167-mmol/L internal standard, 3-trimethylsilyl 2,2,3,3-d4 propionate (TMSP).

Crypt and villus fractions were separated as described earlier and then snap-frozen and stored at -80ºC until sample processing. The modified Bligh and Dyer extraction[46] was used to obtain polar metabolites from the crypt and villus. The samples were homogenized for 30 seconds at 5000 rpm in cold methanol and water with 2.8-mm ceramic beads. Cold chloroform and water were added to the samples to bring the final methanol:chloroform:water ratio to 2:2:1.8. The polar phase was dried by vacuum and resuspended in 600 uL NMR buffer containing 100 mmol/L phosphate buffer, pH 7.3, 1 mmol/L TMSP, and 1 mg/mL sodium azide, prepared in D_2O.

NMR experiments were acquired on a Bruker Avance III HD 600 MHz spectrometer with a 5 mm BBO Prodigy probe (Bruker Analytik, Rheinstetten, Germany). All data were collected at a calibrated temperature of 298 K using the noesygppr1d pulse sequence and processed using Topspin 3.6 software (Bruker Analytik). For a representative sample, 2-dimensional data ^{1}H-^{13}C heteronuclear single quantum coherence were collected to assist with metabolite assignment. A total of 43 metabolites in fecal samples and 34 polar metabolites in epithelial samples were assigned and quantified using Chenomx NMR Suite profiling software (version 8.4; Chenomx, Inc) based on the internal standard, TMSP. The concentrations then were normalized to the tissue weights or the starting material before all statistical analyses and log transformation and mean centering data scaling were used for multivariate analysis. All the metabolomics data analysis were performed using R studio (R Tools Technology) and MetaboAnalyst (University of Alberta).[47]

Western Blot

Protein was extracted from crypt fractions in ice-cold RIPA buffer (#89900; Thermo Scientific) with 0.5 mmol/L EDTA and Halt Protease and Phosphatase inhibitor cocktail (100, #78440; Thermo Scientific), sonicated, and the supernatant was quantified by Pierce BCA assay (Thermo Scientific) before 1:1 dilution in Laemmle buffer containing 2-mercaptoethanol. Protein gels were run according to standard procedure on 4%–12% Bolt Bis-Tris Plus gel (#NW04120BOX; Invitrogen), blocked with Intercept Blocking Buffer (#927-60001; LI-COR), probed with antibodies listed below, and imaged using an Odyssey LI-COR CLx imaging system (Table 3).

scRNA Sequencing

Human intestinal organoids were dissociated and the villus and crypt fractions from each organoid were pooled together. After centrifugation, cells were incubated in 0.05% trypsin-EDTA (#25300054; Thermo Fisher Scientific) for 10 minutes at 37ºC while shaking, washed with 10% FBS, vigorously pipetted to create a single-cell suspension, and then filtered through a 100-mm and 40-mm filter. Filtered cells were centrifuged at 500 $\times$ g for 5 minutes at 4ºC, resuspended in 5% FBS + 0.5% bovine serum albumin+ 10 mm Y-27632 (#1254; Tocris) in PBS and sorted for viability by exclusion of Sytox Blue dead cell stain (#S34857; Thermo Fisher Scientific) on a FACS Aria II (BD). Live cells were collected in 5% FBS + 0.5% bovine serum albumin in PBS, adjusted to a concentration of 10^6 cells/mL. scRNA sequencing library preparation was performed by the Cincinnati Children's Hospital Medical Center Single Cell Genomics Core using the Chromium 3'v3 GEX Kit (10x Genomics). Approximately 12,800 cells were loaded to achieve 8000 captured cells per sample to be sequenced. Sequencing was performed by the Cincinnati Children's Hospital Medical Center DNA Sequencing core using the NovaSeq 6000 (Illumina) sequencing platform with an S2 flow cell to obtain approximately 320 million reads per sample. Raw scRNA sequencing data were converted to FASTQ files and then aligned to the human genome 19 [hg19] using CellRanger v3.0.2 (10x Genomics).

scRNA sequencing data were analyzed using python 3.7.3 via Scanpy (v1.7.0) (Python Software Foundation). After default basic filtering, quality control of samples included cells with a maximum of 8000 genes and with less than 40% mitochondrial-related genes. Default parameters were used for Leiden clustering, visualization via uniform manifold approximation and projection (UMAP), and cluster identification via differential gene expression. Differentially expressed gene lists were generated for each cluster with thresholds of logfold

Table 3. Antibodies Used for Western Blot.

Antibody	Company	Catalog #	Host	Dilution
Tom20 (D8T4N)	Cell Signaling Technology	42406	Rabbit	1:1000
β-actin	Millipore Sigma	A5441	Mouse	1:1000
IRDye 680RD donkey anti-rabbit	LI-COR	926-68073	Donkey	1:15,000
IRDye 800CW donkey anti-mouse	LI-COR	926-32212	Donkey	1:15,000

change greater than 1 and a Wilcoxon adjusted *P* value less than .05. Gene lists were loaded into ToppGene Suite[48] (Cincinnati Children's Hospital Medical Center) to assess overlap with annotated gene ontology lists. Parameters used were false discovery rate (FDR) Benjamini and Hochberg method (B&H) with a cut-off value of 0.05 and a *P* value was calculated using hypergeometric probability mass function.

References

1. Duée P-H, Darcy-Vrillon B, Blachier F, Morel M-T. Fuel selection in intestinal cells. Proc Nutr Soc 1995; 54:83–94.
2. Beumer J, Clevers H. Cell fate specification and differentiation in the adult mammalian intestine. Nat Rev Mol Cell Biol 2021;22:39–53.
3. Gribble FM, Reimann F. Enteroendocrine cells: chemosensors in the intestinal epithelium. Annu Rev Physiol 2016;78:277–299.
4. Lu VB, Rievaj J, O'Flaherty EA, et al. Adenosine triphosphate is co-secreted with glucagon-like peptide-1 to modulate intestinal enterocytes and afferent neurons. Nat Commun 2019;10:1029.
5. Wang J, Cortina G, Wu SV, et al. Mutant neurogenin-3 in congenital malabsorptive diarrhea. N Engl J Med 2006; 355:270–280.
6. Mellitzer G, Beucher A, Lobstein V, et al. Loss of enteroendocrine cells in mice alters lipid absorption and glucose homeostasis and impairs postnatal survival. J Clin Invest 2010;120:1708–1721.
7. McCauley HA, Matthis AL, Enriquez JR, et al. Enteroendocrine cells couple nutrient sensing to nutrient absorption by regulating ion transport. Nat Commun 2020; 11:4791.
8. Ho GT, Theiss AL. Mitochondria and inflammatory bowel diseases: toward a stratified therapeutic intervention. Annu Rev Physiol 2022;84:435–459.
9. Rath E, Moschetta A, Haller D. Mitochondrial function - gatekeeper of intestinal epithelial cell homeostasis. Nat Rev Gastroenterol Hepatol 2018;15:497–516.
10. Stringari C, Edwards RA, Pate KT, et al. Metabolic trajectory of cellular differentiation in small intestine by Phasor Fluorescence Lifetime Microscopy of NADH. Sci Rep 2012;2:568.
11. Schell JC, Wisidagama DR, Bensard C, et al. Control of intestinal stem cell function and proliferation by mitochondrial pyruvate metabolism. Nat Cell Biol 2017;19:1027.
12. Berger E, Rath E, Yuan D, et al. Mitochondrial function controls intestinal epithelial stemness and proliferation. Nat Commun 2016;7:13171.
13. Rodríguez-Colman MJ, Schewe M, Meerlo M, et al. Interplay between metabolic identities in the intestinal crypt supports stem cell function. Nature 2017;543:424.
14. Gao Y, Yan Y, Tripathi S, et al. LKB1 represses ATOH1 via PDK4 and energy metabolism and regulates intestinal stem cell fate. Gastroenterology 2020;158:1389–1401.e10.
15. Ludikhuize MC, Meerlo M, Gallego MP, et al. Mitochondria define intestinal stem cell differentiation downstream of a FOXO/notch axis. Cell Metab 2020; 32:889–900.e7.
16. Perekatt AO, Valdez MJ, Davila M, et al. YY1 is indispensable for Lgr5$^+$ intestinal stem cell renewal. Proc Natl Acad Sci U S A 2014;111:7695–7700.
17. Beyaz S, Mana MD, Roper J, et al. High-fat diet enhances stemness and tumorigenicity of intestinal progenitors. Nature 2016;531:53.
18. Mana MD, Hussey AM, Tzouanas CN, et al. High-fat diet-activated fatty acid oxidation mediates intestinal stemness and tumorigenicity. Cell Rep 2021;35:109212.
19. Yilmaz ÖH, Katajisto P, Lamming DW, et al. mTORC1 in the Paneth cell niche couples intestinal stem-cell function to calorie intake. Nature 2012;486:490.
20. Cheng C-W, Biton M, Haber AL, et al. Ketone body signaling mediates intestinal stem cell homeostasis and adaptation to diet. Cell 2019;178:1115–1131.
21. Mihaylova MM, Cheng C-W, Cao AQ, et al. Fasting activates fatty acid oxidation to enhance intestinal stem cell function during homeostasis and aging. Cell Stem Cell 2018;22:769–778. e4.
22. el Marjou F, Janssen KP, Chang BH, et al. Tissue-specific and inducible Cre-mediated recombination in the gut epithelium. Genesis 2004;39:186–193.
23. Bohin N, Carlson EA, Samuelson LC. Genome toxicity and impaired stem cell function after conditional activation of CreER(T2) in the intestine. Stem Cell Rep 2018; 11:1337–1346.
24. Madisen L, Zwingman TA, Sunkin SM, et al. A robust and high-throughput Cre reporting and characterization system for the whole mouse brain. Nat Neurosci 2010; 13:133–140.
25. Madison BB, Dunbar L, Qiao XT, et al. Cis elements of the villin gene control expression in restricted domains of the vertical (crypt) and horizontal (duodenum, cecum) axes of the intestine. J Biol Chem 2002;277:33275–33283.
26. Urbauer E, Rath E, Haller D. Mitochondrial metabolism in the intestinal stem cell niche—sensing and signaling in health and disease. Front Cell Dev Biol, Published online January 5, 2021, https://doi.org/10.3389/fcell.2020.602814.
27. Liu W, Rodgers GP. Olfactomedin 4 is not a precise marker for human intestinal stem cells, but is involved in intestinal carcinogenesis. Gastroenterology 2022; 162:1001–1004.
28. Spence JR, Mayhew CN, Rankin SA, et al. Directed differentiation of human pluripotent stem cells into intestinal tissue in vitro. Nature 2011;470:105.
29. Watson CL, Mahe MM, Múnera J, et al. An in vivo model of human small intestine using pluripotent stem cells. Nat Med 2014;20:1310.
30. Yu Q, Kilik U, Holloway EM, et al. Charting human development using a multi-endodermal organ atlas and organoid models. Cell 2021;184:3281–3298.e22.
31. Shin ED, Estall JL, Izzo A, et al. Mucosal adaptation to enteral nutrients is dependent on the physiologic actions of glucagon-like peptide-2 in mice. Gastroenterology 2005;128:1340–1353.
32. Chen ME, Naeini SM, Srikrishnaraj A, et al. Glucagon-like peptide-2 stimulates S-phase entry of intestinal Lgr5+ stem cells. Cell Mol Gastroenterol Hepatol 2022; 13:1829–1842.

33. Rock SA, Jiang K, Wu Y, et al. Neurotensin regulates proliferation and stem cell function in the small intestine in a nutrient-dependent manner. Cell Mol Gastroenterol Hepatol 2022;13:501–516.
34. El-Salhy M, Danielsson A, Stenling R, Grimelius L. Colonic endocrine cells in inflammatory bowel disease. J Intern Med 1997;242:413–419.
35. Lien G-S, Lin C-H, Yang Y-L, et al. Ghrelin induces colon cancer cell proliferation through the GHS-R, Ras, PI3K, Akt, and mTOR signaling pathways. Eur J Pharmacol 2016;776:124–131.
36. Ławnicka H, Mełeń-Mucha G, Motylewska E, et al. Modulation of ghrelin axis influences the growth of colonic and prostatic cancer cells in vitro. Pharmacol Rep 2012;64:951–959.
37. Koehler JA, Kain T, Drucker DJ. Glucagon-like peptide-1 receptor activation inhibits growth and augments apoptosis in murine CT26 colon cancer cells. Endocrinology 2011;152:3362–3372.
38. Brown RE, Short SP, Williams CS. Colorectal cancer and metabolism. Curr Colorectal Cancer Rep 2018;14:226–241.
39. Bhattacharyya A, Chattopadhyay R, Mitra S, Crowe SE. Oxidative stress: an essential factor in the pathogenesis of gastrointestinal mucosal diseases. Physiol Rev 2014;94:329–354.
40. McGrath PS, Watson CL, Ingram C, et al. The basic helix-loop-helix transcription factor NEUROG3 is required for development of the human endocrine pancreas. Diabetes 2015;64:2497–2505.
41. Zhang X, McGrath PS, Salomone J, et al. A comprehensive structure-function study of neurogenin3 disease-causing alleles during human pancreas and intestinal organoid development. Dev Cell 2019;50:367–380.e7.
42. Múnera JO, Wells JM. Generation of gastrointestinal organoids from human pluripotent stem cells. Organ regeneration. Springer, 2017:167–177.
43. Bas T, Augenlicht LH. Real time analysis of metabolic profile in ex vivo mouse intestinal crypt organoid cultures. J Vis Exp 2014;93:52026.
44. Fan Y-Y, Davidson LA, Callaway ES, et al. A bioassay to measure energy metabolism in mouse colonic crypts, organoids, and sorted stem cells. Am J Physiol Gastrointest Liver Physiol 2015;309:G1–G9.
45. Moon C, VanDussen KL, Miyoshi H, Stappenbeck TS. Development of a primary mouse intestinal epithelial cell monolayer culture system to evaluate factors that modulate IgA transcytosis. Mucosal Immunol 2014;7:818–828.
46. Wu H, Southam AD, Hines A, Viant MR. High-throughput tissue extraction protocol for NMR- and MS-based metabolomics. Anal Biochem 2008;372:204–212.
47. Xia J, Wishart DS. Using MetaboAnalyst 3.0 for comprehensive metabolomics data analysis. Curr Protoc Bioinformatics 2016;55:14.10.1–14.10.91.
48. Chen J, Bardes EE, Aronow BJ, Jegga AG. ToppGene Suite for gene list enrichment analysis and candidate gene prioritization. Nucleic Acids Res 2009;37(Suppl 2):W305–W311.

Received October 4, 2022. Accepted December 27, 2022.

Correspondence
Address correspondence to: Heather A. McCauley, PhD, Department of Cell Biology and Physiology, University of North Carolina at Chapel Hill School of Medicine, 111 Mason Farm Road, Chapel Hill, North Carolina 27599. e-mail: heather_mccauley@med.unc.edu.

Acknowledgments
The authors would like to acknowledge the assistance of the ^{1}H-NMR Metabolomics Core in the Division of Pathology and Laboratory Medicine, the Research Flow Cytometry Core in the Division of Rheumatology, and the Single Cell Genomics Core in the Division of Developmental Biology at Cincinnati Children's Hospital Medical Center.

CRediT Authorship Contributions
Heather A McCauley, PhD (Conceptualization: Lead; Data curation: Lead; Formal analysis: Lead; Funding acquisition: Supporting; Investigation: Lead; Methodology: Lead; Project administration: Lead; Resources: Supporting; Supervision: Lead; Validation: Lead; Visualization: Lead; Writing – original draft: Lead; Writing – review & editing: Lead)
Anne Marie Riedman, n/a (Data curation: Supporting; Formal analysis: Supporting; Investigation: Supporting; Methodology: Supporting; Validation: Supporting; Visualization: Supporting)
Jacob Ryan Enriquez, BS (Data curation: Supporting; Formal analysis: Supporting; Investigation: Supporting; Methodology: Supporting; Validation: Supporting; Visualization: Supporting)
Xinghao Zhang, PhD (Formal analysis: Supporting; Investigation: Supporting; Visualization: Supporting)
Miki Watanabe-Chailland, PhD (Data curation: Supporting; Formal analysis: Supporting; Methodology: Supporting; Visualization: Supporting)
Jose Guillermo Sanchez, BS (Data curation: Supporting; Formal analysis: Supporting; Investigation: Supporting; Methodology: Supporting; Validation: Supporting; Visualization: Supporting)
Daniel O Kechele, PhD (Data curation: Supporting; Formal analysis: Supporting; Investigation: Supporting; Methodology: Supporting)
Emily F Paul, n/a (Data curation: Supporting; Methodology: Supporting)
Kayle Riley, BS (Methodology: Supporting)
Courtney Burger, PhD (Methodology: Supporting)
Richard A Lang, PhD (Methodology: Supporting)
James M Wells, PhD (Conceptualization: Supporting; Formal analysis: Supporting; Funding acquisition: Lead; Resources: Lead; Supervision: Supporting; Writing – review & editing: Supporting)

Conflicts of interest
The authors disclose no conflicts.

Funding
This project was supported by National Institutes of Health grants 1K01 DK125341 (H.A.M.), U19 AI116491 (J.M.W.), P01 HD093363 (J.M.W.), and UH3 DK119982 (J.M.W.); the Shipley Foundation (J.M.W.); and the Allen Foundation (J.M.W.). This project also was supported in part by the Digestive Diseases Research Core Center in Cincinnati (National Institutes of Health grant P30 DK078392).

Data Availability Statement
Single-cell sequencing data are available in GEO (accession #GSE214852). All other data are available upon request.